THE GEOLOGICAL SOCIETY OF AMERICA®

Dynamic weakening and amorphization in serpentinite during laboratory earthquakes

Nicolas Brantut[1], François X. Passelègue[2], Damien Deldicque[2], Jean-Noël Rouzaud[2], and Alexandre Schubnel[2]
[1]Rock & Ice Physics Laboratory and Seismological Laboratory, Department of Earth Sciences, University College London, Gower Street, London WC1E 6BT, UK
[2]Laboratoire de Géologie, CNRS UMR 8538, École Normale Supérieure, 24 rue Lhomond, 75005 Paris, France

ABSTRACT

The mechanical properties of serpentinites are key factors in our understanding of the dynamics of earthquake ruptures in subduction zones, especially intermediate-depth earthquakes. Here, we performed shear rupture experiments on natural antigorite serpentinite, which showed that friction reaches near-zero values during spontaneous dynamic rupture propagation. Rapid coseismic slip (>1 m/s), although it occurs over short distances (<1 mm), induces significant overheating of microscale asperities along the sliding surface, sufficient to produce surface amorphization and likely some melting. Antigorite dehydration occurs in the fault walls, which leaves a partially amorphized material. The water generated potentially contributes to the production of a low-viscosity pressurized melt, explaining the near-zero dynamic friction levels observed in some events. The rapid and dramatic dynamic weakening in serpentinite might be a key process facilitating the propagation of earthquakes at intermediate depths in subduction zones.

INTRODUCTION

Serpentinites are formed by hydrothermal alteration of upper mantle ultramafic rocks, and they are found in several key tectonic environments (Hirth and Guillot, 2013). In subduction zones, the presence of antigorite (the high-pressure polymorph of serpentine minerals) has been inferred along the subducting interface (e.g., Deschamps et al., 2013) and is often considered to be the host rock of intermediate-depth earthquakes (e.g., Hacker et al., 2003).

A precise knowledge of the mechanical properties of antigorite during dynamic rupture propagation, and especially of the associated microscale deformation mechanisms, is therefore essential to understand the dynamics of earthquake ruptures along major intermediate-depth seismogenic faults. Early laboratory investigations (Reinen et al., 1994; Moore et al., 1997) showed that antigorite is frictionally stable, i.e., velocity-strengthening, when tested under typical subduction zone conditions and slip rates comparable to tectonic plate velocities. However, recent studies have provided evidence that antigorite weakens significantly, with coefficients of friction as low as 0.1 (Hirose and Bystricky, 2007; Kohli et al., 2011; Proctor et al., 2014), when deformed at slip rates comparable to those inferred during earthquake slip (several cm/s and above). Such weakening has commonly been interpreted as the macroscopic manifestation of a process called flash heating (e.g., Rice, 2006), which, in the case of hydrous minerals such as serpentines, arises from the thermal dehydration reaction into talc, olivine, and water at microscale asperities along the frictional interface (Kohli et al., 2011; Proctor et al., 2014).

However, all our current knowledge is based on friction experiments performed exclusively under imposed, constant slip rate conditions, and the precise impact of the observed weakening on the dynamics of rupture remains to be determined. In addition, flash heating mechanisms remain poorly constrained by the existing laboratory tests, which are run for slip distances of at least several tens of centimeters (Proctor et al., 2014), i.e., several orders of magnitudes larger than the typical size of surface asperities. As a result, the early stage of dynamic friction (the first few tens of microns of slip), which provides a key control on rupture dynamics (Brantut and Rice, 2011), is yet to be determined.

We performed stick-slip experiments in saw-cut samples of natural antigorite under triaxial stress conditions (i.e., for principal stresses such that $\sigma_2 = \sigma_3 < \sigma_1$) at confining pressures of σ_3 = 30 and 95 MPa (resulting in fault-normal stresses of up to >200 MPa, i.e., much higher than allowed in a typical rotary shear apparatus). Individual stick-slip events are spontaneous dynamic slip instabilities similar to earthquake ruptures (Brace and Byerlee, 1966; Johnson and Scholz, 1976), and hence they allow us to test directly how the frictional properties of antigorite impact rupture dynamics. A network of piezoelectric transducers was positioned around the simulated fault, allowing measurements of rupture speed (Passelègue et al., 2013), while the dynamic shear stress evolution was measured using an amplified full-bridge strain gauge recorded at 10 MHz (Passelègue et al., 2014).

METHODS

The material chosen for this study was an antigorite-rich serpentinite from Corsica (France), taken from the same block as the one used by Gasc et al. (2011). It is mostly composed of Mg-rich antigorite, with an Fe/(Fe + Mg) ratio of ~0.03 (measured using energy-dispersive X-ray spectroscopy). Minor traces of Fe and Ni oxides preexist in the rock, located along foliation planes.

Two cylindrical samples of 40 mm diameter and 90 mm length were cored along the same direction from the block, and then saw-cut at 30° from their long axis. The saw-cut surfaces were roughened with coarse sandpaper (grit number #240, ~50 µm roughness), using ethanol to avoid frictional heating during the process.

A 350 Ω full-bridge strain gauge was bonded on the side of the sample, as close as possible to the saw-cut plane (Fig. DR1 in the GSA Data Repository[1]). The orientation of the strain gauge bridge was chosen so that the bridge would record the net differential stress $\sigma_1 - \sigma_3$. The sample was then placed in a nitrile jacket equipped with 14 piezoelectric transducers. The geometry of the sensor array is shown in Figure DR1.

The samples were placed into a triaxial deformation apparatus (e.g., Brantut et al., 2011). Stick-slip events were produced by imposing a constant shortening rate on the sample, equivalent to a net slip rate of 8 µm/s across the saw cut. The signals from the piezoelectric transducers were recorded, unamplified, with a 10 MHz digital oscilloscope. The signal from the strain gauge was amplified and recorded using two dedicated oscilloscope channels. The voltage measured from the amplified strain gauge was calibrated

[1]GSA Data Repository item 2016197, description of the method used to estimate rupture speed, and supplementary figures, is available online at www.geosociety.org/pubs/ft2016.htm, or on request from editing@geosociety.org.

and converted into differential stress by matching the measured axial load during the elastic loading stage at the beginning of each experiment (prior to the onset of frictional sliding).

The resolved shear and normal stresses on the fault plane were computed from both the static stress (from the externally measured axial load) and the dynamic in situ stress (from the strain gauges), and the friction coefficient was computed from those resolved stresses (transient changes in the fault-normal stress were therefore accounted for). Transient changes in confining pressure were neglected, which is justified by the relatively high compliance of the confining medium.

The rupture speed during stick-slip events was estimated using the methodology given by Passelègue et al. (2013), which uses the array of piezoelectric transducers to track the rupture front arrival time (see the GSA Data Repository).

EXPERIMENTAL RESULTS

We observed a total of five stick-slip events in the test performed at 95 MPa confining pressure and 13 stick-slip events in the test performed at 30 MPa confining pressure. The events initiated at relatively high shear stress (friction coefficients ranging from 0.65 up to 1.03) and produced displacements ranging from 30 µm up to 1.03 mm (Fig. 1A; Fig. DR2), which correspond to equivalent moment magnitudes ranging from M_w −3.9 to M_w −2.9. The events systematically generated high-amplitude acoustic emissions (Fig. DR3), and we estimate rupture speeds ranging from 3.5 km/s (sub-Raleigh) up to 6.5 km/s (supershear, near P-wave speed). During each event, the local stress measured near the fault plane dropped rapidly over a time period of the order of a few tens of microseconds (Fig. 1B). The magnitude of the initial dynamic stress drop was generally comparable to the initial shear stress measured immediately prior to the event. For eight of the 18 events recorded in our experiments, the dynamic stress drop was nearly equal to the initial stress, indicating a total strength loss and effectively a momentarily frictionless motion across the interface. By contrast, the static stress drop (as recorded, at a rate of 1 Hz, on the external measurement of axial stress; see Fig. 1A) was much less than the dynamic stress drop, by around a factor of 2. An example of a full stress-time record is given in Figure DR4, which shows that the final stress immediately after rupture remained close to the minimum dynamic stress level, and that the increase to the "long-term" static value (as recorded by our external stress measurement) occurred over much larger time scales than those of the rupture events.

In addition, for some of the large events (numbers 1, 2, and 4 in Fig. 1B), a second rapid stress drop was also observed at ~180 µs after the first stress drop, indicating a second dynamic rupture. Such secondary ruptures might originate from reflections on the sample-piston interfaces of the strong elastic waves generated by the first main rupture; we therefore only discuss here the characteristics of the first rupture events.

From the measured minimum dynamic stress, and assuming a constant confining pressure during sliding, an estimate for the minimum dynamic friction coefficient can be computed. Concurrently, the peak slip rate can be estimated from two independent quantities. First, we use the dynamic stress drop $\Delta\tau_{dyn}$ (computed from the change in the resolved dynamic shear stress), which is known to scale with the peak slip rate (Johnson and Scholz, 1976; Brune, 1970) following

$$v \approx v_r \frac{\Delta\tau_{dyn}}{G/(1-\nu)}, \quad (1)$$

where v_r is the rupture speed, G is the shear modulus, and ν is Poisson's ratio of the rock. Second, we use the measured total slip (δ) over the weakening time (t_w, measured from the dynamic stress measurement as the time interval from peak to minimum stress) and estimate the slip rate as $v \approx \delta/t_w$, which is an upper bound for the average slip rate (since only a fraction of the total slip occurs during the weakening phase). Both estimates demonstrate that the dynamic friction coefficient decreases dramatically and reaches near-zero values with increasing slip rate (Fig. 2), indicating a very strong velocity-weakening behavior over slip displacements of less than a few tenths of a millimeter at most.

Furthermore, a plot of the dynamic friction coefficient as a function of the initial resolved shear stress prior to rupture (Fig. DR5) shows that dynamic friction decreases dramatically with increasing initial shear stress. In other words, events that occurred at high stresses tended to produce more complete dynamic stress drops.

Scanning electron microscope (SEM) observations of the slip surfaces after the experiments revealed the presence of a highly porous, foam-like material that formed flow structures aligned with the direction of slip (Figs. 3A and 3B). These surface textures were found pervasively on the sliding surface, although a precise quantitative estimate of the actual surface area they covered was not possible due to the high level of magnification required to detect them. By contrast, the surface texture observed in a sample deformed under similar pressure conditions, but unloaded before any stick-slip event occurred, did not show any foam-like or flow structures, only grooving and grain size reduction (Fig. DR6).

The matrix also contains micron- to submicron-sized Fe-oxide angular clasts (light gray/white particles in Figs. 3A and 3B). In order to gain further insights into the internal structure

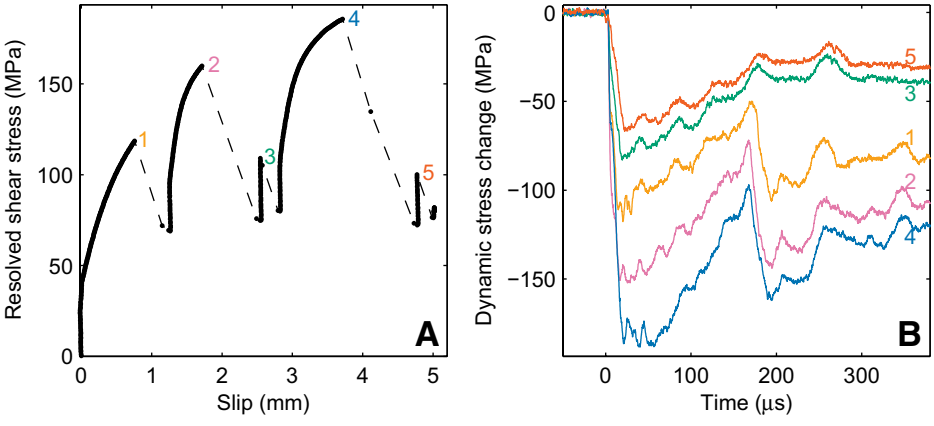

Figure 1. Stick-slip events during antigorite friction at a confining pressure of 95 MPa. A: Resolved shear stress as a function of slip displacement along the simulated fault in antigorite. Dashed lines correspond to stick-slip events, during which stress drops and slip is too rapid to be captured by low-frequency (1 Hz) recording of data. B: Records of resolved dynamic shear stress changes during each stick-slip event, recorded at 10 MHz from a strain gauge bridge positioned near the fault. Numbers and colors correspond to the events marked in A.

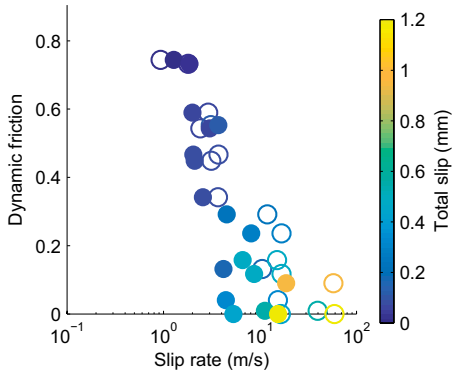

Figure 2. Estimate of dynamic friction as a function of slip rate. Open symbols correspond to slip rates estimated from ratio of total slip and weakening time, and filled symbols correspond to slip rates estimated from rupture speed multiplied by ratio of dynamic stress drop and modified shear modulus.

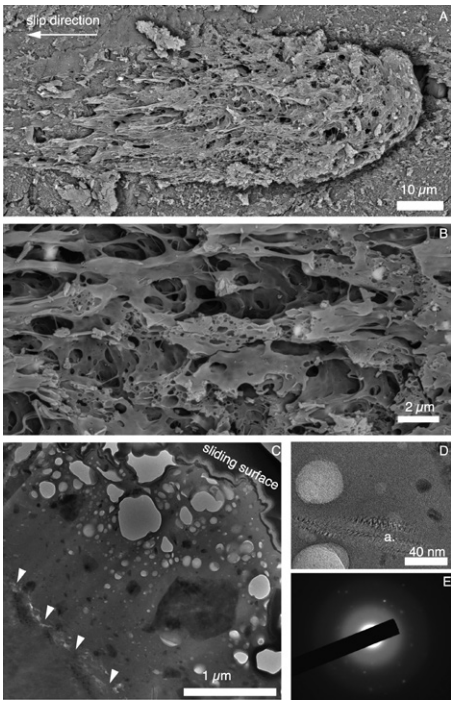

Figure 3. Micro- and nanostructures along the slip surface. A–B: Scanning electron microscope backscattered-electron observation showing (A) a sheared asperity, and (B) coating foam-like matrix and Fe-oxide clasts (white patches) underneath the surface. C: Transmission electron microscope (TEM) image of focused ion beam (FIB) section cut perpendicular to slip surface. Arrows indicate limit between amorphized matrix and intact material. Pores/bubbles appear in light gray. D: High-resolution TEM image of coating matrix near interface with intact antigorite. A fragment of antigorite (a) is present, in which Bragg fringes indicate lattice distortion. E: Selected area electron diffraction pattern of the matrix, showing diffusion rings indicative of an amorphous matrix as well as a number of diffraction spots revealing crystalline grains within section thickness.

of the surface matrix, an ultrathin section was fabricated across the slip surface, perpendicular to the direction of slip, using a focused ion beam (FIB). Transmission electron microscope (TEM) analysis of the section (Fig. 3C) shows a clear distinction between the foam-like matrix, which contains Fe-oxide clasts (observed as darker grains), and the underlying intact antigorite. The thickness of the matrix layer is of the order of 1 to 3 μm, and a strong gradient in porosity is observed from the bottom of the layer, which contains only small pores or bubbles (of a few tens of nanometers at most), to the top of the layer (i.e., at the sliding interface), where large (up to several hundreds of nanometers) and numerous pores are observed. Near the interface with the intact antigorite, the matrix contains fragments of deformed antigorite (Fig. 3D), whereas no such fragments could be detected near the sliding interface. Selected area electron diffraction patterns indicate that the matrix is mostly amorphous (Fig. 3E) and has nanometer-sized crystals embedded, as shown by the faint spots in the diffraction pattern. We found no clear evidence for the presence of any of the known dehydration reaction products of antigorite (recrystallized olivine, enstatite, or talc), which indicates that the dehydration reaction occurred too fast for the conventional mineral reaction products to recrystallize significantly in these samples. Complementary analysis using X-ray powder diffraction on the collected surface gouge confirmed that, if they are present, the potential reaction products of antigorite remain below the detection limit, while the amorphous material is clearly detected (Fig. DR7). Moreover, the average elementary composition of the foam-like matrix, analyzed with energy-dispersive X-ray spectroscopy under the SEM, was found to be depleted in oxygen compared to the initial composition of the intact antigorite (Fig. DR8), which indicates an overall lower content in structural water.

DISCUSSION AND CONCLUSIONS

In order to test whether the transformation of antigorite into olivine and talc or enstatite is at all possible during the stick-slip events, we computed an estimate of the reaction progress at the asperity contacts using the framework of flash heating (Rice, 2006; Rempel and Weaver, 2008) and laboratory-derived kinetics (Gualtieri et al., 2012).

Initially assuming negligible reaction progress, the temperature T_a along asperity contacts during sliding at constant slip rate v is given by

$$T_a(t) = T_0 + (\tau_c v)/(\rho C)\sqrt{t/(\pi\alpha_{th})}, \quad (2)$$

where T_0 is the ambient temperature in the surrounding rock (here assumed to be room temperature), τ_c is the shear strength of the asperity, ρC is the heat capacity, equal to 2.49 MPa/°C for antigorite, t is time, and α_{th} (= 1.04 mm^2/s) is the thermal diffusivity of antigorite (Rempel and Weaver, 2008). The strength τ_c was estimated from the product of the friction coefficient and the constant normal stress given as a function of the Moh hardness H as $0.123 \times H^{2.3}$ GPa (Beeler et al., 2008). The friction coefficient involved in the computation of τ_c is a local one at the asperity contact; following Bowden and Tabor (1964), this local friction coefficient is considered equal to the macroscopic measured friction. Here, we used the average of the friction coefficients measured immediately prior to stick-slip events in all our experiments, which is 0.86. Based on an average hardness $H = 3.75$ for antigorite (cf. http://www.mindat.org database), the computed asperity shear stress is thus τ_c = 2.2 GPa. From the temperature evolution with time $T_a(t)$, we computed the reaction progress ξ from first-order kinetics as

$$\xi(t) = 1 - \exp\left(-\int_0^t \kappa\{T(t')\}\,dt'\right), \quad (3)$$

where $\kappa(T)$ is the thermally activated kinetic parameter of the dehydration reaction, given as $\kappa(T) = A\exp(-E_a/RT)$, $A \approx 6.55 \times 10^{12}$/s, and $E_a \approx 255$ kJ/mol (Gualtieri et al., 2012). The extent of the reaction was estimated from Equation 3 at either end of the asperity lifetime, given by D_a/v for an asperity of size D_a sliding at constant slip rate v, or, if it came first, at the onset of melting, using a prospective melting point taken as 990 °C, which is the average solidus temperature for a wet basic rock assemblage at pressures between 0.2 and 3 GPa (Iwamori, 1998).

For slip rates above 1 m/s, which is a lower bound for the peak slip rate achieved during most of the stick-slip events, the computed reaction progress (Fig. 4) remains negligible, and the asperity contacts are expected to melt before dehydration occurs. This result is consistent with our SEM and TEM observations, and it indicates that the amorphous foam-like matrix is likely a frozen melt. In that hypothesis, the observed micro- and nanopores and bubbles in the matrix could originate from the rapid degassing of the hydrous melt formed from antigorite, a process similar to that observed during high-pressure shock melting of hydrous phases (Lambert and Lange, 1984). Whether or not the amorphization of antigorite originates from a melting process, its relatively lower water content compared to the intact material is clear evidence for the loss of structural water through a devolatilization process. The amorphization allows free water to form, which may contribute to the dynamic weakening by either generating a local fluid

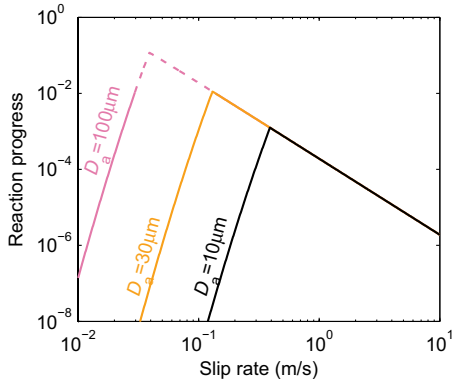

Figure 4. Estimated maximum reaction extent at asperity contacts as a function of slip rate. For a given asperity size D_a, reaction extent is first limited by asperity lifetime and increases with increasing slip rate, up to a critical velocity, beyond which it becomes limited by 990 °C isotherm, where we assume the contact melts. Dotted lines correspond to computed reaction extents greater than 1%, above which latent of heat of reaction (neglected here) should contribute significantly.

pressure, or, in the case of melting, dramatically decreasing the viscosity of the melt.

Our micro- and nanostructural observations show that devolatilization occurred in a thin layer around the sliding surface, while intact material was found directly in contact with this layer. An order-of-magnitude estimate of the thermal gradient can be found assuming that the top layer is at the melting temperature of 990 °C, and using a heat diffusion length of $\sqrt{\alpha_{th} \times t_w} \approx 4.5$ μm (using a heat diffusivity $\alpha_{th} = 1$ mm^2/μs and a weakening time $t_w =$ 20 μs): The resulting gradient is of the order of 200 °C/mm. At a distance of 2 μm from the melt layer, the temperature is therefore less than 600 °C, which is compatible with the presence of stable antigorite.

Our results show that the onset of dynamic slip in antigorite is governed by the partial amorphization or melting, and devolatilization of structural water at microscale asperity contacts. The overall mechanical behavior is strongly velocity weakening and so is qualitatively consistent with the theory of flash heating (Rice, 2006; Beeler et al., 2008). The conventional dehydration reaction into olivine and talc or enstatite is likely too slow to prevent melting at asperity contacts, but devolatilization occurs off the sliding surface, leaving a partially amorphized material. This process is similar to that observed during high-pressure shock melting of hydrous phases (Lambert and Lange, 1984). The release of water potentially contributes to the near-zero dynamic friction by either decreasing the melt viscosity, hydrous melts being generally much less viscous than anhydrous melts of the same composition (e.g., Hui and Zhang, 2007), or increasing the local pore fluid pressure, if free water forms as bubbles in the slipping zone (Fig. 3; see also Proctor et al., 2014).

The large slip, stress drops, and high rupture speeds recorded during the stick-slip events in antigorite show that this mineral does not constitute a barrier to earthquake ruptures, but it may in fact facilitate earthquake propagation. While the early stages of slip are marked by dramatic weakening by flash amorphization or melting, coupled with devolatilization near the slip surface, the later stages (for slip larger than a few centimeters) are likely to be affected by bulk dehydration (Hirose and Bystricky, 2007; Kohli et al., 2011; Proctor et al., 2014) and the resulting thermo-chemical pressurization (Brantut et al., 2010). As a result, the shear resistance of antigorite is likely near zero during seismic slip, if a high enough background stress can be accumulated across the fault prior to rupture (as in the case of our experiments, see Fig. 2; Fig. DR5). These weakening mechanisms operative at high slip rates in antigorite provide an explanation for the occurrence of large intermediate-depth earthquakes, which are considered to originate and propagate through serpentine-rich layers in subduction zones.

ACKNOWLEDGMENTS

This work was supported by the Natural Environment Research Council (grant NE/K009656/1 to Brantut) and the Agence Nationale pour la Recherche (project "DELF" ANR-12-JS06–0003 to Schubnel). We thank Takehiro Hirose, Hiroki Sone, Brooks Proctor, and Greg Hirth for their constructive review comments.

REFERENCES CITED

Beeler, N.M., Tullis, T.E., and Goldsby, D.L., 2008, Constitutive relationships and physical basis of fault strength due to flash heating: Journal of Geophysical Research, v. 113, p. B01401, doi:10.1029/2007JB004988.

Bowden, F.P., and Tabor, D., 1964, The Friction and Lubrication in Solids, Volume 2: Oxford, UK, Oxford University Press, 544 p.

Brace, W.F., and Byerlee, J.D., 1966, Stick-slip as a mechanism for earthquakes: Science, v. 153, p. 990–992, doi:10.1126/science.153.3739.990.

Brantut, N., and Rice, J.R., 2011, How pore fluid pressurization influences crack tip processes during dynamic rupture: Geophysical Research Letters, v. 38, p. L24314, doi:10.1029/2011GL050044.

Brantut, N., Schubnel, A., Corvisier, J., and Sarout, J., 2010, Thermochemical pressurization of faults during coseismic slip: Journal of Geophysical Research, v. 115, p. B05314, doi:10.1029/2009JB006533.

Brantut, N., Han, R., Shimamoto, T., Findling, N., and Schubnel, A., 2011, Fast slip with inhibited temperature rise due to mineral dehydration: Evidence from experiments on gypsum: Geology, v. 39, p. 59–62, doi:10.1130/G31424.1.

Brune, J.N., 1970, Tectonic stress and the spectra of seismic shear waves from earthquakes: Journal of Geophysical Research, v. 75, p. 4997–5009, doi:10.1029/JB075i026p04997.

Deschamps, F., Godard, M., Guillot, S., and Hattori, K., 2013, Geochemistry of subduction zone serpentinites: A review: Lithos, v. 178, p. 96–127, doi:10.1016/j.lithos.2013.05.019.

Gasc, J., Schubnel, A., Brunet, F., Guillon, S., Mueller, H.-J., and Lathe, C., 2011, Simultaneous acoustic emissions monitoring and synchrotron X-ray diffraction at high pressure and temperature: Calibration and application to serpentinite dehydration: Physics of the Earth and Planetary Interiors, v. 189, p. 121–133, doi:10.1016/j.pepi.2011.08.003.

Gualtieri, A.F., Giacobbe, C., and Viti, C., 2012, The dehydroxylation of serpentine group minerals: The American Mineralogist, v. 97, p. 666–680, doi:10.2138/am.2012.3952.

Hacker, B.R., Peacock, S.M., Abers, G.A., and Holloway, S.D., 2003, Subduction factory 2. Are intermediate-depth earthquakes in subducting slabs linked to metamorphic dehydration reactions?: Journal of Geophysical Research, v. 108, p. 2030, doi:10.1029/2001JB001129.

Hirose, T., and Bystricky, M., 2007, Extreme dynamic weakening of faults during dehydration by coseismic shear heating: Geophysical Research Letters, v. 34, p. L14311, doi:10.1029/2007GL030049.

Hirth, G., and Guillot, S., 2013, Rheology and tectonic significance of serpentinite: Elements (Quebec), v. 9, p. 107–113, doi:10.2113/gselements.9.2.107.

Hui, H., and Zhang, Y., 2007, Toward a general viscosity equation for natural anhydrous and hydrous silicate melts: Geochimica et Cosmochimica Acta, v. 71, p. 403–416, doi:10.1016/j.gca.2006.09.003.

Iwamori, H., 1998, Transportation of H_2O and melting in subduction zones: Earth and Planetary Science Letters, v. 160, p. 65–80, doi:10.1016/S0012-821X(98)00080-6.

Johnson, T.L., and Scholz, C.H., 1976, Dynamics properties of stick-slip friction of rock: Journal of Geophysical Research, v. 81, p. 881–888, doi:10.1029/JB081i005p00881.

Kohli, A.H., Goldsby, D.L., Hirth, G., and Tullis, T., 2011, Flash weakening of serpentinite at near-seismic slip rates: Journal of Geophysical Research, v. 116, p. B03202, doi:10.1029/2010JB007833.

Lambert, P., and Lange, M.A., 1984, Glasses produced by shock melting and devolatilization of hydrous silicates: Journal of Non-Crystalline Solids, v. 67, p. 521–542, doi:10.1016/0022-3093(84)90174-1.

Moore, D.E., Lockner, D.A., Shengli, M., Summers, R., and Byerlee, J.D., 1997, Strengths of serpentinite gouges at elevated temperatures: Journal of Geophysical Research, v. 102, no. B7, p. 14,787–14,801, doi:10.1029/97JB00995.

Passelègue, F.X., Schubnel, A., Nielsen, S., Bhat, H.S., and Madariaga, R., 2013, From sub-Rayleigh to supershear ruptures during stick-slip experiments on crustal rocks: Science, v. 340, p. 1208–1211, doi:10.1126/science.1235637.

Passelègue, F.X., Goldsby, D.L., and Fabbri, O., 2014, The influence of ambient fault temperature on flash-heating phenomena: Geophysical Research Letters, v. 41, p. 828–835, doi:10.1002/2013GL058374.

Proctor, B.P., Mitchell, T.M., Hirth, G., Goldsby, D., Zorzi, F., Platt, J.D., and Di Toro, G., 2014, Dynamic weakening of serpentinite gouge and bare-surfaces at seismic slip rates: Journal of Geophysical Research, v. 119, p. 8107–8131, doi:10.1002/2014JB011057.

Reinen, L.A., Weeks, J.D., and Tullis, T.E., 1994, The frictional behavior of lizardite and antigorite serpentinites: Experiments, constitutive models, and implications for natural faults: Pure and Applied Geophysics, v. 143, p. 317–358, doi:10.1007/BF00874334.

Rempel, A.W., and Weaver, S.L., 2008, A model for flash weakening by asperity melting during high-speed earthquake slip: Journal of Geophysical Research, v. 113, p. B11308, doi:10.1029/2008JB005649.

Rice, J.R., 2006, Heating and weakening of faults during earthquake slip: Journal of Geophysical Research, v. 111, p. B05311, doi:10.1029/2005JB004006.

Manuscript received 25 March 2016
Revised manuscript received 29 May 2016
Manuscript accepted 1 June 2016

Printed in USA

Supplementary materials for: Dynamic weakening and amorphisation during laboratory earthquakes in serpentinite

Nicolas Brantut[1], François X. Passelègue[2], Damien Deldicque[2]
Jean-Noël Rouzaud[2] & Alexandre Schubnel[2]

[1] *Rock & Ice Physics Laboratory and Seismological Laboratory, Department of Earth Sciences, University College London, Gower Street, London, WC1E 6BT, UK.*
[2] *Laboratoire de Géologie, CNRS UMR 8538, École Normale Supérieure, 24 rue Lhomond, 75005 Paris, France.*

1 Estimation of Rupture Speed

Arrival times were picked automatically form the raw waveforms using a method based on the Akaike Information Criterion, with a precision (checked by comparing with manual picks) of the order of 1 μs. The forward problem consists in a simple model for the rupture front arrival time, in which the rupture is assumed to be either circular (for sub-Rayleigh rupture speeds) or elliptical (for super-shear rupture speeds). The theoretical arrival time at station i, denoted t_i, is computed as

$$t_i = t_0 + \sqrt{\frac{(x-x_i)^2}{c_{III}^2} + \frac{(y-y_i)^2}{c_{II}^2}}, \tag{1}$$

where t_0 is the origin time of the rupture, (x,y) are the coordinates of its initiation point in the fault plane, c_{II} (resp. c_{III}) is the rupture speed in the in-plane (resp. out of plane) direction, and (x_i,y_i) are the coordinates of the station. The inverse problem consists in determining the model parameters x, y, t_0, c_{II}, and c_{III}. We used a generic grid-search approach, sweeping through all potential values for each parameter, and computing a likelihood function based on the least absolute value criterion. For simplicity we assumed a circular rupture front ($c_{II} = c_{III}$) for sub-Rayleigh ruptures ($c_{II} < c_s$), and assumed that $c_{III} = c_s$ during supershear ruptures. In the inversion we used a constant value of the shear wave speed $c_s = 3.83$ km/s.

2 Supplementary Figures

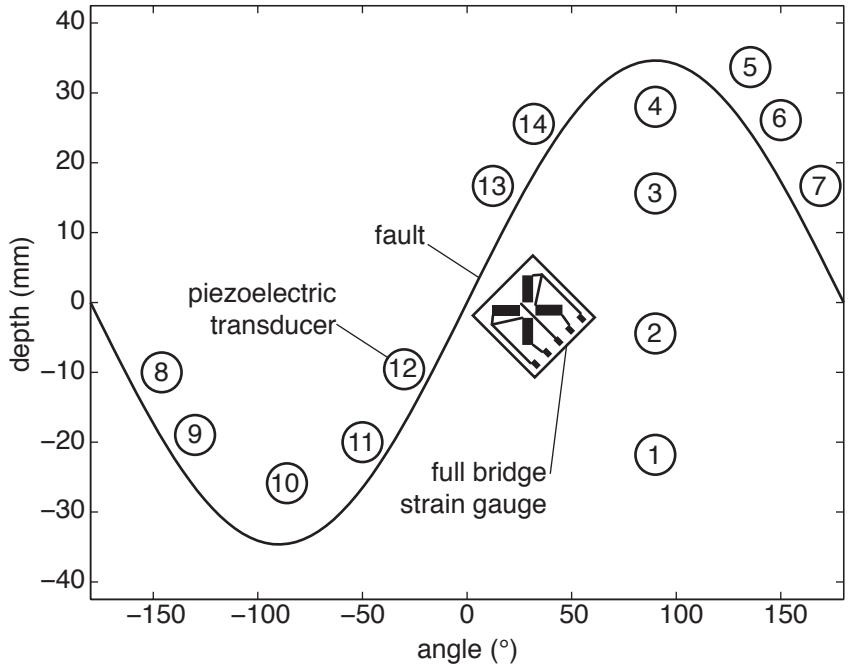

Figure DR1: Schematic of the sensor arrangement and strain gauge positioning around the sample. The sensor positions for the samples deformed at 95 and 30 MPa confining pressure were almost identical, with minor variations due to the manual fabrication of the perforated jacket

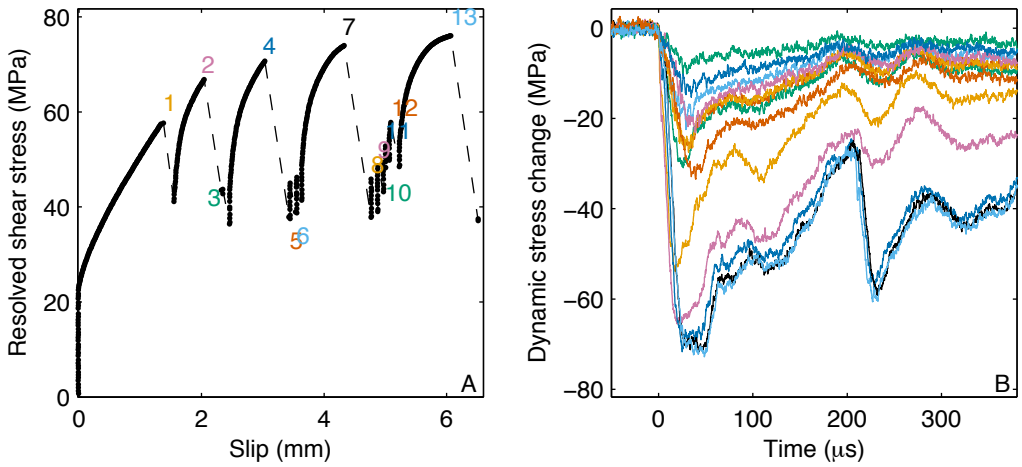

Figure DR2: Stick-slip events during antigorite friction at a confining pressure of 30 MPa. (A) Resolved shear stress as a function of slip displacement along the simulated fault in antigorite. The dashed lines correspond to stick-slip events, during which stress drops and slip is too rapid to be captured by the low frequency (1 Hz) recording of the data. (B) Records of dynamic stress changes during each stick slip event, recorded at 10 MHz from a strain gauge bridge positioned near the fault. Numbers and colors correspond to the events marked in panel A.

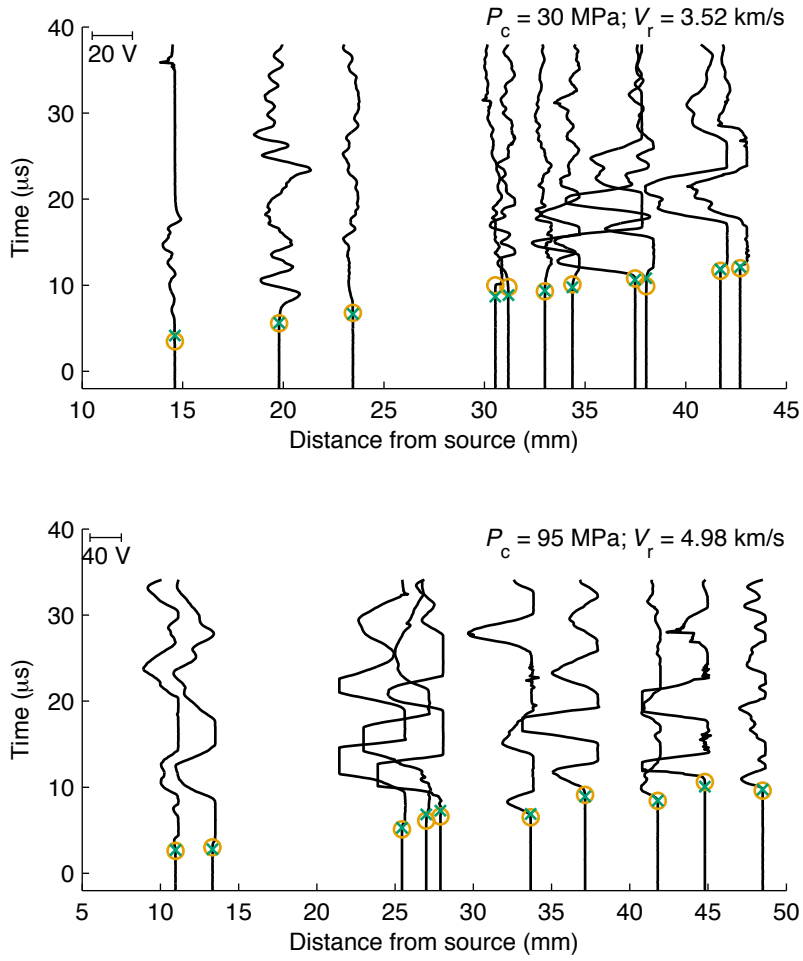

Figure DR3: Representative examples of waveforms recorded on the piezoeletric transducers during two stick-slip events, which were inferred to propagate at subshear (top) and supershear (bottom) rupture speeds. Orange circles mark picked rupture arrival times, and green crosses mark computed theoretical arrival times. Traces for each sensor are plotted as a function of the distance to the source location.

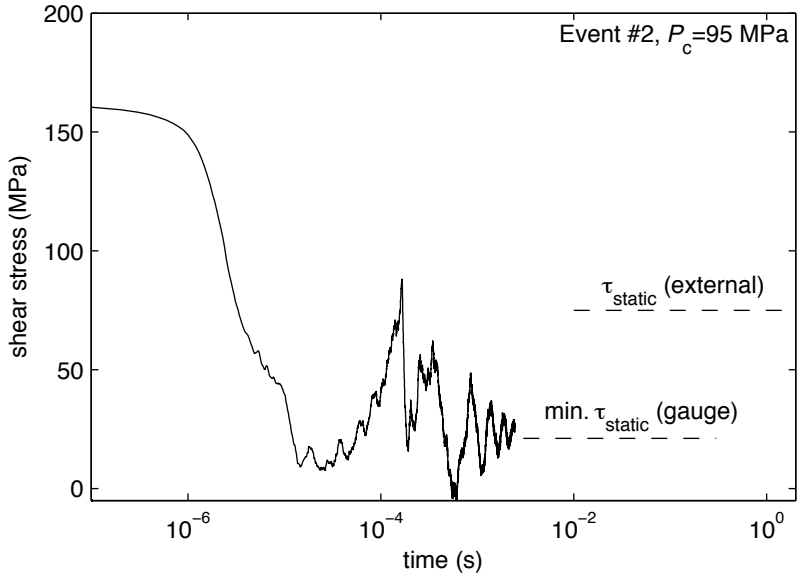

Figure DR4: Representative example of a full length stress-time time record, corresponding to event number 2 recorded in the experiment performed at $P_c = 95$ MPa. The dashed line marked with τ_{static} (gauge) corresponds to the stress level measured by the full bridge strain gauge immediately after the rupture event, recorded at a 10 Hz sampling rate. The dashed line marked with τ_{static} (external) corresponds to the stress level measured externally at the end of the loading column, recorded at 1 Hz.

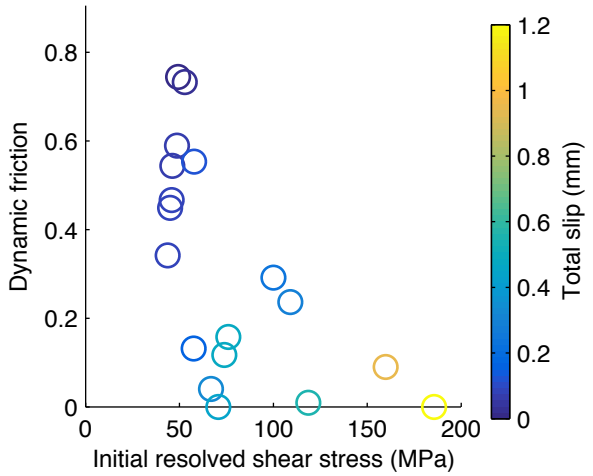

Figure DR5: Dynamic friction coefficient as a function of the initial resolved shear stress on the fault plane immmediately prior to stick-slip events. There is a clear trend towards decreasing (and even vanishing) dynamic friction coefficient with increasing initial shear stress.

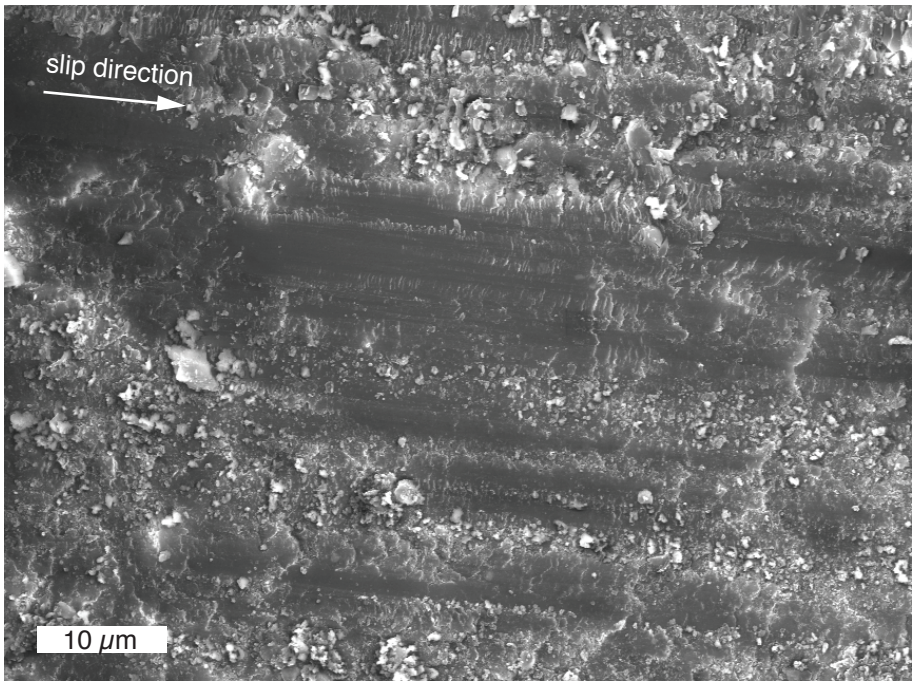

Figure DR6: SEM secondary electron image of the sliding surface of a pre-cut antigorite sample deformed at 60 MPa confining pressure but unloaded before any stick-slip event occurred. The surface texture is markedly different from that observed after stick-slip events, and shown only grooving and grain size reduction. No foam-like material or flow structures could be observed.

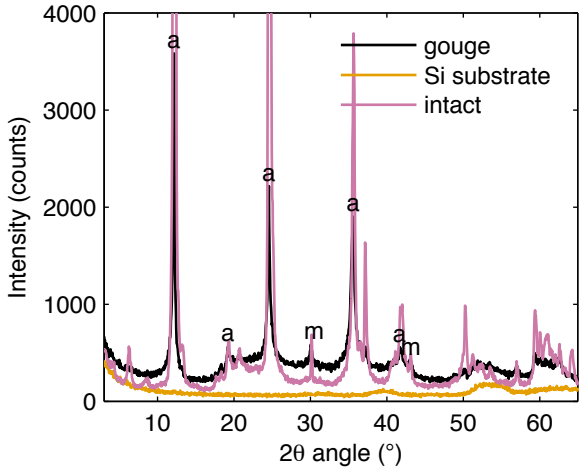

Figure DR7: X-ray powder diffraction pattern of the collected surface gouge after the experiment at 95 MPa confining pressure. The gouge was collected by shaking one half of the faulted sample in an alcohol bath using ultrasounds, and letting the alcohol evaporate from the bath. No further grinding was used. The measurement was performed using a silicon substrate. Antigorite peaks (a), as well as magnetite peaks (m; already present in the intact material) appear very clearly, but no significant other crystalline phase can be detected. By contrast with both the Si substrate alone (shown in orange) and the intact antigorite (shown in pink), the gouge pattern also contains a clear bump between 15 and 45 degrees, which indicates the presence of amorphous material.

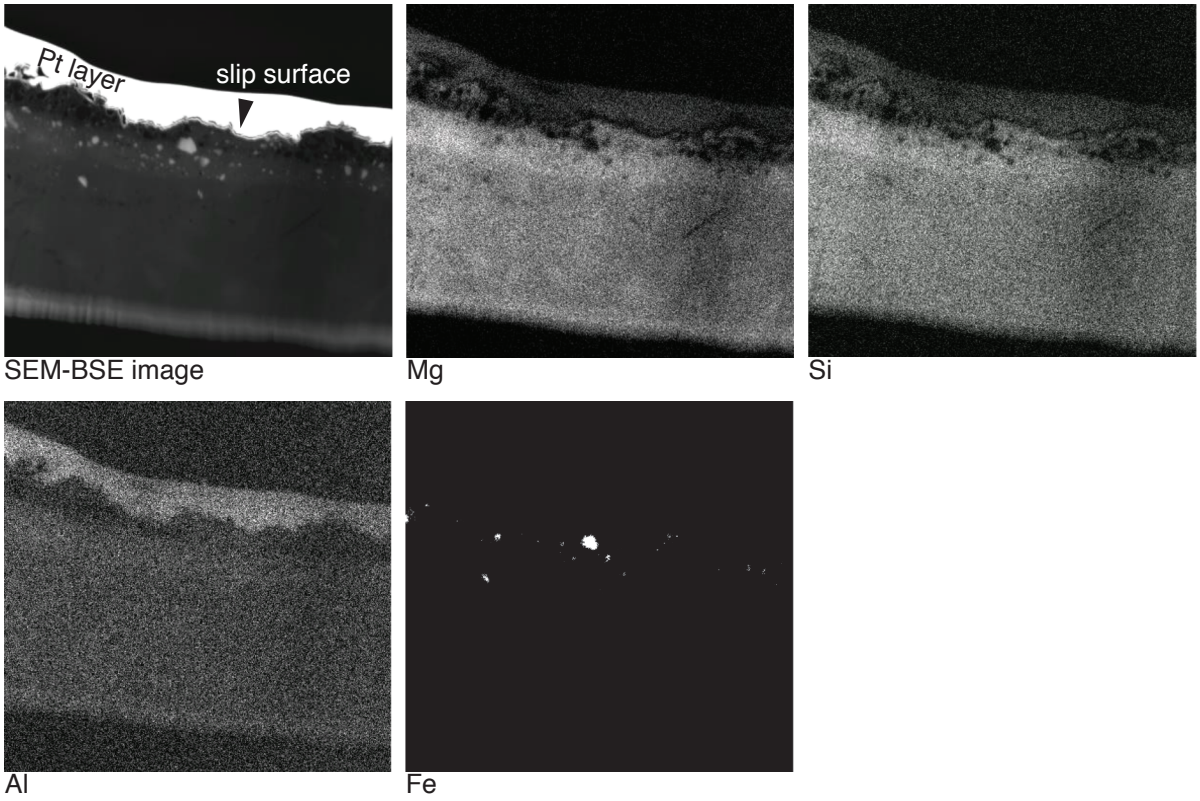

Figure DR8: Chemical composition analysis of the FIB section using energy dispersive x-ray spectroscopy under the SEM. The top left image is a backscattered electron image of the section, and the other images are elemental maps of magnesium (Mg), silicon (Si), aluminum (Al) and iron (Fe). The relative abundance of each element is indicated by the color scale, from black (element is absent) to white (very abundant). There is a distinct layer beneath the slip surface in which all major elements are more abundant than below, which indicates a lower concentration in oxygen, which can be explained by devolatilisation of structural water from the initial antigorite.